Journal of Ceramic Processing Research. Vol. 26, No. 6, pp. 975~985 (2025)
(Received 22 July 2025, Received in revised form 5 October 2025, Accepted 12 October 2025)
https://doi.org/10.36410/jcpr.2025.26.6.975

JOURNAL OF
Ceramic Processing Research

Mechanical properties of porcelain insulator enhanced with spherical mullite powders

Yonggang Yue[a],*, Xiaoyun Tian[a], Xiaochuan Chong[b], Donghai Ding[b], Guoqing Xiao[b], Liming Wang[c], Bin Cao[c] and Lanjun Yang[d]
[a] *Inner Mongolia Ultra High Voltage Power Supply Branch, Inter Mongolia Power (Group) Co., Ltd., Hohhot 010080, China*
[b] *College of Materials Science and Engineering, Xi'an University of Architecture and Technology, Xi'an 710055, China*
[c] *Tsinghua Shenzhen International Graduate School, Shenzhen 518055, China*
[d] *School of Electrical Engineering, Xi'an Jiaotong University, Xi'an 710055, China*

To enhance the mechanical properties of high-voltage porcelain insulator, the columnar mullite agglomerated spherical powder was introduced as a reinforcing phase. High-alumina based porcelain insulator containing varying spherical mullite powder contents (0–30 wt.%) were fabricated by cold isostatic pressing. The effects of reinforcing phase content on physical and mechanical properties, phase composite and microstructure were investigated, and the underlying strengthening and toughening mechanisms were elucidated. The results show that the 12 wt.% spherical mullite powders (S12) added sample exhibited optimal overall properties. The compressive strength and flexural strength of S12 reached 321 MPa and 107 MPa, respectively, showing an obvious improvement over the reference sample S0. Especially, the fracture toughness of S12 increased by 45.4% to 5.1 MPa·m$^{1/2}$ and the critical crack size improved by 60.1% to 714 μm compared with S0. Microstructural analysis revealed that the original columnar mullite in spherical particles interlaced with in-situ generated mullite forming a three-dimensional interlocking network. The formed unique microstructure effectively absorbed elastic strain energy and suppressed crack propagation, achieving strengthening and toughening of the porcelain insulators.

Keywords: Porcelain insulators, Spherical mullite powders, Enhancing and toughening.

Introduction

Porcelain insulators are key foundational materials that support the safe and stable operation of power systems [1, 2]. With the rapid development of the power industry, the operating conditions of porcelain insulators are becoming increasingly stringent, thus the high-performance high-voltage porcelain insulators is necessary. Continuously improving the insulation level of materials is required to meet higher voltage levels, while enhancing their ability to resist pollution flashover and brittle fracture to adapt to complex working environments [3, 4]. As indispensable components in power systems, like other ceramic materials, the inherent brittleness of porcelain insulators is a significant factor in its explosion and damage during operation [5]. Especially for traditional porcelain insulators predominantly composed of alumina or quartz, due to their inherent brittleness and microstructural defects, it is difficult to simultaneously meet the requirements for high strength and toughness, which is particularly evident under extreme operating conditions [6-9].

Due to the limitations of optimizing raw material formulations and preparation processes in enhancing insulators, researchers have begun to explore the incorporation of reinforcing phases to optimize microstructural characteristics and improve mechanical properties [10-12]. Esmaili et al. [13] investigated the effects of micro/nano TiO_2 doping on the densification behavior and mechanical properties of porcelains. They demonstrated that the samples containing 5 wt.% micro/nano TiO_2 had the highest densification and Vickers microhardness. Contreras et al. [14] studied the influence of the incorporation of nano-alumina on the microstructure, mechanical properties of siliceous porcelain. The results showed that the addition of nano-Al_2O_3 promote the mechanical strengthening due to the increment of mullite. The cold crushing and flexural strength of the porcelain system were enhanced by 14.6% and 36%, respectively, compared with conventional porcelain. Mehta et al. [15] found that the mechanical property of porcelain is improved with the addition of $BaTiO_3$, the bending, tensile and compressive strength values of porcelains sintered at 1350 °C enhanced by 2.1%, 1.3% and 3.1%, respectively, compare with the reference samples. These studies collectively confirm that introducing reinforcing phases effectively regulates

---

*Corresponding author:
Tel : +86-15947713617
Fax: +86-15947713617
E-mail: hvyue@163.com

ceramic microstructures and activates toughening mechanisms such as crack deflection and bridging

Mullite ($3Al_2O_3 \cdot 2SiO_2$), with its exceptional high-temperature stability, low thermal expansion coefficient, and chemical compatibility with alumina matrices [16, 17]. One-dimensional morphology mullite are predominantly incorporated into ceramic matrices as reinforcing phases to enhance the mechanical properties of ceramics [18-20]. These morphologies can be introduced either through external addition or in-situ synthesis during composite fabrication. There are also some studies that improve the mechanical properties of insulators by regulating the formation of mullite [21]. However, the application of acicular mullite in high-voltage porcelain insulators has been severely constrained by its poor distribution uniformity and weak interfacial bonding strength with the matrix, which collectively compromise mechanical reliability under operational stresses [22-24].

Columnar mullite agglomerated spherical powder featuring an interwoven network structure composed of glassy phase-bonded columnar mullite crystals not only retains the inherent advantages of columnar mullite but also mitigates whisker agglomeration through its unique architectural design [25]. When employed as a novel reinforcing phase, the molten glassy phase during sintering interacts with Al_2O_3 in ceramic raw materials generated in-situ mullite, and synergistically with the original columnar mullite to form a distinctive three-dimensional network configuration [26-29]. Such structural engineering is anticipated to substantially enhance ceramic performance by optimizing stress distribution and crack propagation resistance [30].

In this study, columnar mullite agglomerated spherical powder were employed as the raw material, and its effects on the mechanical properties of high-alumina based porcelain insulator was investigated. The influence of spherical mullite content on compressive strength, flexural strength, and fracture toughness was comprehensively evaluated. Finally, the underlying strengthening and toughening mechanisms induced by spherical mullite were elucidated through microstructural characterization of the specimens.

Experimental

Raw materials and samples preparation

The raw materials including ceramic matrix material (CM, particle size <250 μm, Xi'an XD High-Voltage Electroceramic Co., Ltd.), columnar mullite agglomerated spherical powder (MS, named as spherical mullite powder, particle size <100 μm, Hunan Jiashunhua Advanced Materials Co., Ltd.), and potassium feldspar (PS, purity ≥99.5 wt.%, particle size <80 μm), and 1 wt.% polyvinyl alcohol (PVA) aqueous solution was incorporated as a binder. The microstructure of spherical mullite shows in Fig. 1. It can be seen that the glass phase in spherical mullite is wrapped around mullite, and mullite has a rod-shaped structure. The detailed chemical compositions of all raw materials are detailed in Table 1.

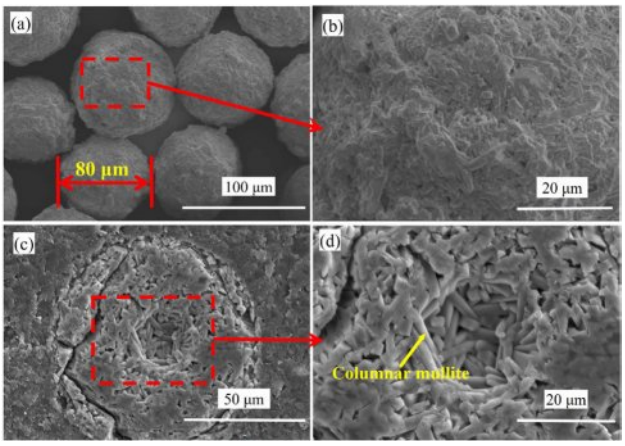

Fig. 1. SEM images of columnar mullite agglomerated spherical powder: (a-b) surface, (c-d) cross-sectional.

Preparation and characterization

The columnar mullite agglomerated spherical powder were coated with a mixed powder of porcelain matrix material and potassium feldspar through dry granulation process. The porcelain matrix material and potassium feldspar were subjected to 10-hour ball milling pretreatment. After that, the volume ratio between coated spherical mullite and mixture raw materials was controlled at 1:1. And 1 wt.% polyvinyl alcohol (PVA) solution was employed as binder to achieve homogeneous coating of the mixed powder on spherical mullite through mortar mixing. The coated composite particles were subsequently mixed with the remaining porcelain matrix material in proportions specified in Table 2, with the chemical compositions of the mixtures detailed in Table 3. The mixed powders were uniaxially pressed at 50 MPa for 2 minutes to form green ceramic compacts with dimensions of Φ20 mm × 20 mm (cylindrical) and 3 × 4 × 40 mm (rectangular). Following cold isostatic pressing at 105 MPa for 5 minutes, the green bodies

Table 1. Chemical composition of different raw materials (wt.%).

Raw materials	Al_2O_3	SiO_2	CaO	Na_2O	Fe_2O_3	MgO	K_2O	TiO_2	LOI
CM	32.9	56.6	0.4	0.4	1.1	0.15	2.9	2.1	2.9
MS	61.21	34.25	1.82	0	0	0	0	2.72	0.57
PS	20	66	0.2	0.5	0.4	10.6	2.3	0	0.44

Table 2. Proportion of raw materials.

Sample number	Raw material ratio(wt.%)		
	CM	MS	PS
S0	100	0	-
S6	94	6	2
S12	88	12	2
S18	82	18	2
S24	76	24	2
S30	70	30	2

Table 3. Chemical composition of the mixed porcelain insulator raw materials.

Sample number	Content (wt.%)			
	Al_2O_3	SiO_2	Fe_2O_3	K_2O
S0	56.60	32.90	1.10	2.90
S6	56.15	33.63	1.12	2.88
S12	56.43	33.69	1.17	2.71
S18	56.69	33.76	1.21	2.55
S24	56.95	33.83	1.25	2.39
S30	57.21	33.90	1.29	2.23

were sintered in a medium-temperature furnace to obtain porcelain specimens. And 5 samples were prepared for each test group.

The phase composition of specimens was characterized using an X-ray diffractometer (XRD, D/MAX 2400, Rigaku, Japan) with Cu-Kα radiation. Field emission scanning electron microscopy coupled with energy-dispersive spectroscopy (FESEM-EDS, SU6600, Hitachi Ltd., Tokyo, Japan) was employed to examine the morphology and microstructure of specimens, with simultaneous elemental analysis performed via EDS. The bulk density and apparent porosity were determined based on Archimedes method. Mechanical properties were evaluated through three-point bending tests (30 mm span, 0.5 mm/min loading speed) and compressive strength measurements using a universal testing machine (YAM 2000 B, Jinan Tianchen Testing Machine Technology Co., China). Micromechanical parameters were conducted via nanoindentation tests (TriboIndenter TI980, Hysitron, USA) to determine hardness and elastic modulus. Vickers hardness measurements were performed with a diamond pyramid indenter (HV-1000B, Shanghai Taiming Optical Instrument Co., China) under 5 kg load with 10 s dwell time. Subsequent SEM observations of indentation morphology enabled calculation of Vickers hardness (Hv) and fracture toughness (K_{IC}) through crack length analysis. Furthermore, the crack evolution during fracture processes was achieved using an ultrasonic testing system (RAEM1-1) equipped with 10 MHz transducers.

Results and Discussion

Phase and microstructure

The phase composition of sintered porcelain insulator samples was characterized by XRD, and the result is shown in Fig. 2. All sintered samples exhibited corundum and mullite as their predominant phases. With the increase in spherical mullite content, the intensity ratio between the strongest characteristic peaks of corundum and mullite progressively decreased, indicating that the introduced spherical mullite powder effectively increase the mullite content in the samples.

Furthermore, the microstructural characteristics of sintered porcelain insulator were investigated through SEM. Fig. 3 distinctly reveals the pore distribution features within the samples. A notable trend emerged where the pore population initially decreased before subsequently increasing with higher spherical mullite additions. This bimodal behavior originates from the unique structural configuration of spherical mullite, which comprises interwoven rod-like mullite crystals. At moderate addition levels (≤12 wt.%), the rod-like constituents from spherical mullite synergistically interacted with in-situ formed acicular mullite to establish a three-dimensional network architecture. This interpenetrating structure demonstrated superior pore-filling capability, complemented by the intrinsic pore-occupying effect of spherical mullite particles. Particularly at 12 wt.% spherical mullite addition, the samples achieved optimal densification with minimal observable porosity in both pore dimensions and population. However, excessive additions (>12 wt.%) induced particle agglomeration of spherical mullite, compromising the structural homogeneity and consequently deteriorating the microstructure through pore coalescence and increased porosity. Additionally, the formation of in-situ mullite was accompanied by volumetric expansion during sintering, and excessive volume expansion can increase the pores

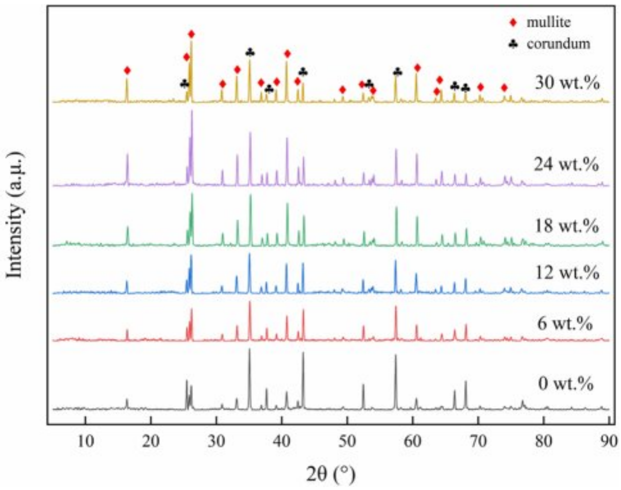

Fig. 2. XRD results of the samples with different content of spherical mullite powders.

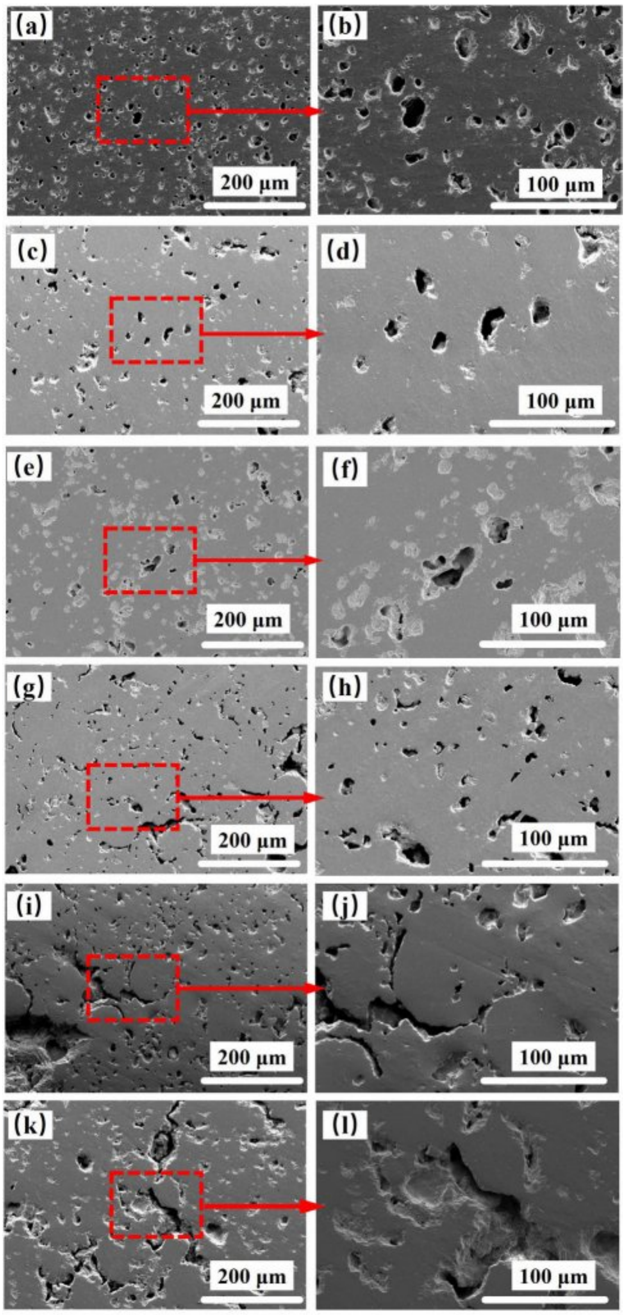

Fig. 3. SEM images of the samples with different content of spherical mullite powders: (a-b) 0 wt.%, (c-d) 6 wt.%, (e-f) 12 wt.%, (g-h) 18 wt.%, (i-j) 24 wt.%, (k-l) 30 wt.%

and defects within the samples.

Physical properties

The physical properties of ceramic specimens sintered with varying spherical mullite additions were investigated. As illustrated in Fig. 4, the bulk density (BD) and apparent porosity (AP) of ceramic specimens exhibited contrasting evolutionary trends. The BD demonstrated an initial increase followed by a subsequent decrease, while the AP conversely displayed a decrease-to-increase transition. This counteractive behavior can be attributed to the dual effects of spherical mullite incorporation. Submicron spherical mullite particles effectively filled interparticle voids during the initial stage (≤12 wt.%), thereby enhancing particle packing efficiency to simultaneously elevate BD and reduce AP. However, excessive additions (>12 wt.%) induced self-agglomeration of fine particles, disrupting the ordered stacking arrangement and ultimately diminishing BD.

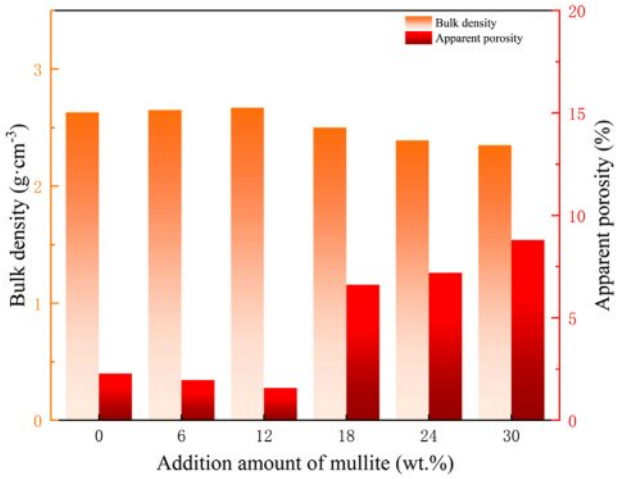

Fig. 4. Bulk density and apparent porosity of the samples with different content of spherical mullite powders.

Simultaneously, the progressive increase in mullite content elevated the glass phase concentration. The transient liquid phase formed during initial sintering stages facilitated particle rearrangement and pore elimination through viscous flow mechanisms. Nevertheless, beyond critical concentration thresholds, excessive glass phase accumulation hindered solid-state diffusion processes while exacerbating interparticle friction and residual stresses, collectively contributing to AP increase. Furthermore, the interfacial reaction between Al_2O_3 and SiO_2 during sintering generated secondary mullite, a process accompanied by 3-5% volumetric expansion. While this reaction partially compensated for porosity formation, it simultaneously undermined the densification process, emerging as a principal factor in BD reduction.

The synergistic effect of these mechanisms leads to a critical conclusion from Fig. 4: Spherical mullite additions exceeding 12 wt.% induce detrimental effects characterized by 11.9% BD deterioration (from 2.67 to 2.35 g/cm^3) and 461% AP elevation (from 1.57% to 8.80%), establishing 12 wt.% as the optimal addition threshold for microstructural optimization.

The water absorption rate (WA) exhibited analogous variation trends to AP, reaching its minimum value of 0.7% at 12 wt.% spherical mullite addition. This optimization can be attributed to the optimal mullite incorporation that facilitated particle rearrangement and created homogeneous liquid-phase distribution, effectively reducing porosity while enhancing densification efficiency. However, exceeding 12 wt.% mullite content triggered concurrent increases in both AP and WA, where excessive mullite disrupted matrix continuity, impeded densification kinetics, and ultimately elevated open porosity through microstructural discontinuity.

The linear shrinkage rate (LS) evolution further elucidated the changing trend of BD. A progressive decline in LS accompanied increasing mullite content, primarily ascribed to the volumetric expansion effect (4-8%) associated with the mullitization reaction ($3Al_2O_3 + 2SiO_2 \rightarrow 3Al_2O_3 \cdot 2SiO_2$) [31, 32]. This reaction-induced expansion partially counterbalanced sintering shrinkage through two mechanisms: (1) crystalline phase transformation involving volume increase during mullite formation, and (2) anisotropic growth of acicular mullite grains generating internal compressive stresses. The resultant dimensional compensation effect fundamentally modified the shrinkage-stress equilibrium, thereby reducing net densification while maintaining dimensional stability.

Compressive strength and flexural strength

The compressive strength of sintered porcelain insulator samples with varying additions of spherical mullite is presented in Fig. 7. The compressive strength results demonstrate a strong correlation with AP and the pore distribution characteristics observed by SEM, where elevated porosity content corresponds to diminished mechanical property. Specifically, the compressive strength of porcelain insulators exhibited an initial enhancement with increasing spherical mullite content, reaching an optimal value of 321 MPa when 12 wt.% spherical mullite is introduced. However, a progressive decline in compressive strength was observed when the mullite content exceeded this amount. Notably, the 30

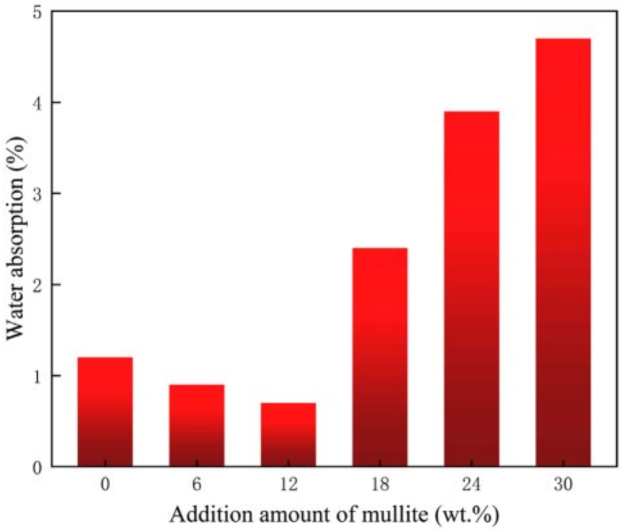

Fig. 5. Water absorption rate of the samples with different content of spherical mullite powders.

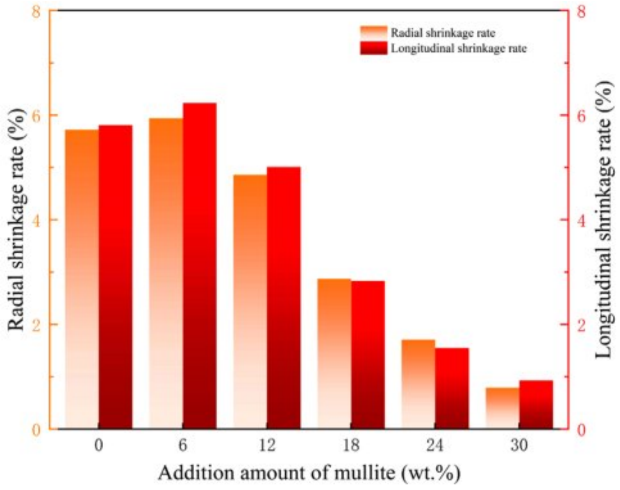

Fig. 6. Linear shrinkage rate of the samples with different content of spherical mullite powders.

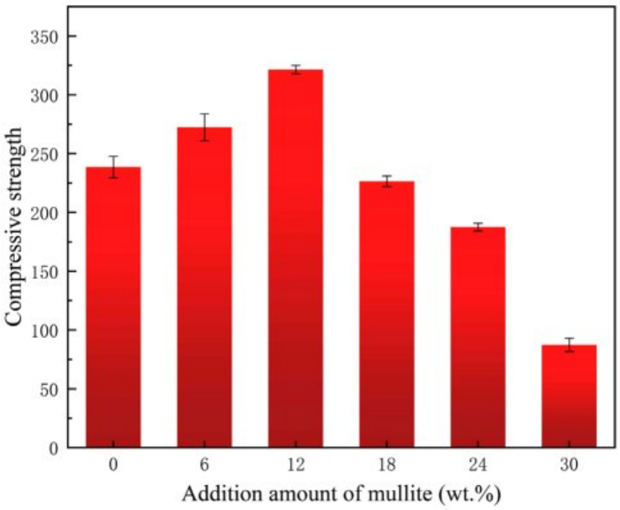

Fig. 7. Compressive strength of the samples with different content of spherical mullite powders.

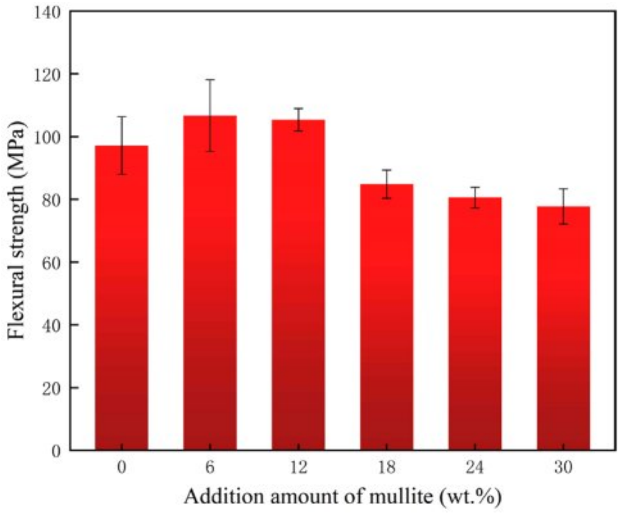

Fig. 8. Flexural strength of the samples with different content of spherical mullite powders.

wt.% spherical mullite added specimen manifested the lowest compressive strength of 87 MPa, attributable to insufficient densification during sintering processing.

The mechanical properties of the sample are closely related to its microstructure. According to the SEM images, the peak strength at 12 wt.% mullite addition corresponds to the minimal and small-sized pore, where spherical mullite particles effectively function as reinforcing fillers while maintaining structural integrity. Conversely, both deficient and excessive mullite induced detrimental porosity development through distinct mechanisms: insufficient mullite content permits uncontrolled pore coalescence during sintering, while excessing disrupts particle packing efficiency and creating more interparticle

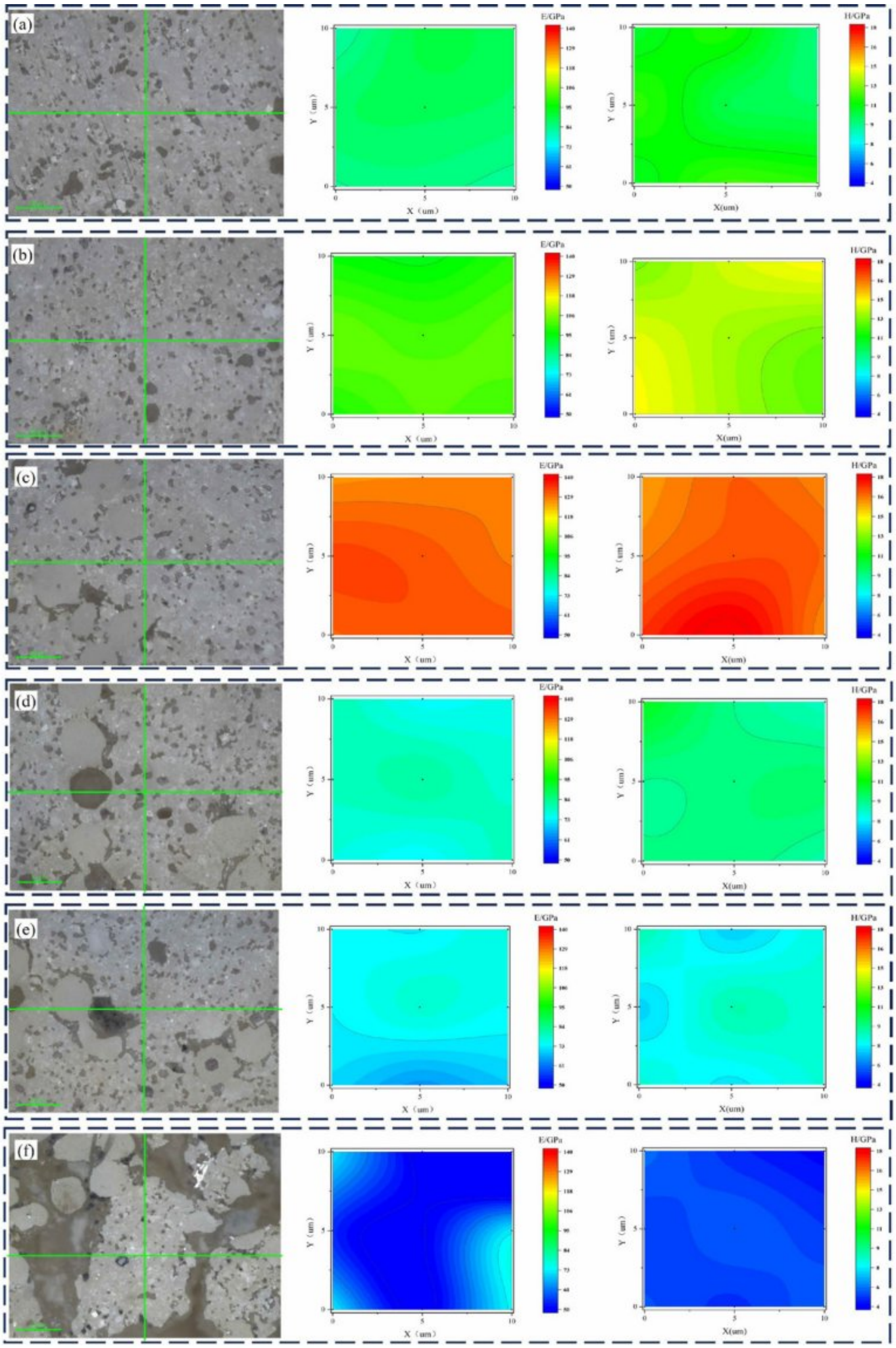

Fig. 9. Photo of nanoindentation area and corresponding micromechanical parameter cloud diagram of samples with different content of spherical mullite powders: (a-b) 0 wt.%, (c-d) 6 wt.%, (e-f) 12 wt.%, (g-h) 18 wt.%, (i-j) 24 wt.%, (k-l) 30 wt.%.

voids. All of these conclusively demonstrate that mullite content, distribution and morphology are critical for balancing porosity and strength in insulating ceramics.

The flexural strength of sintered porcelain insulators with graded spherical mullite additions are illustrated in Fig. 8. Within the range of 0-12 wt.% mullite content, the specimens exhibited a progressive enhancement in flexural strength. Notably, comparable peak values of approximately 107 MPa were achieved at both 6 wt.% and 12 wt.% mullite additions. When it exceeds 12 wt.%, however, a marked deterioration in mechanical strength was observed, culminating in a minimum flexural strength of 77.8 MPa at 30 wt.% mullite content.

This strength evolution pattern demonstrates remarkable consistency with the previously observed compressive strength behavior (Fig. 7), with both mechanical parameters exhibiting strong inverse correlations with the material's AP. The congruence in these trends substantiates the critical role of porosity modulation in governing the strength of insulators. Specifically, the dual-peak phenomenon at 6 wt.% and 12 wt.% additions suggest the existence of competing mechanisms: initial porosity reduction through mullite-induced densification at lower concentrations, and then at 12%, the increase in in-situ mullite whisker content plays a major positive role. These findings collectively show that it is necessary to control the introduction of mullite content in order to balance the enhancement efficiency and microstructural stability when enhancing insulators.

Micromechanics parameters

The micromechanics parameters of elastic modulus and hardness for sintered porcelain insulators with varying spherical mullite additions were measured by nanoindentation. To ensure the reliability of the results, randomly select a 3×3 matrix for each sample to test, obtain a micro-area mechanical parameter cloud diagram, and calculate the equivalent values of different parameters based on multi-point data [33]. The test area photos and corresponding micro-area hardness and elastic modulus cloud diagram of different samples are shown in Fig. 9.

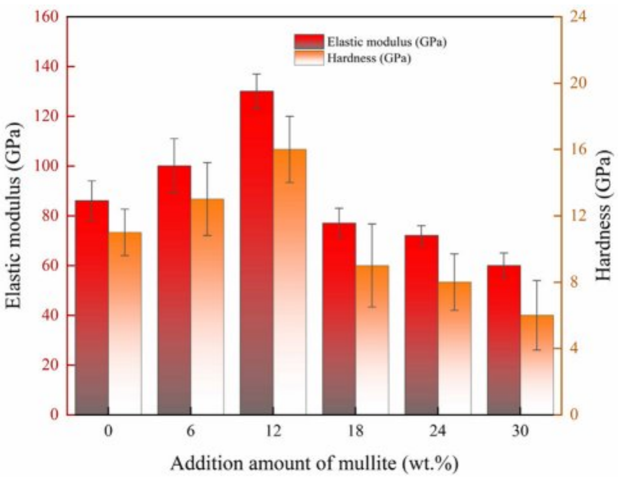

Fig. 10. Elastic modulus and hardness obtained by nanoindentation of the samples with different content of spherical mullite powders.

It can be seen that when the addition amount of

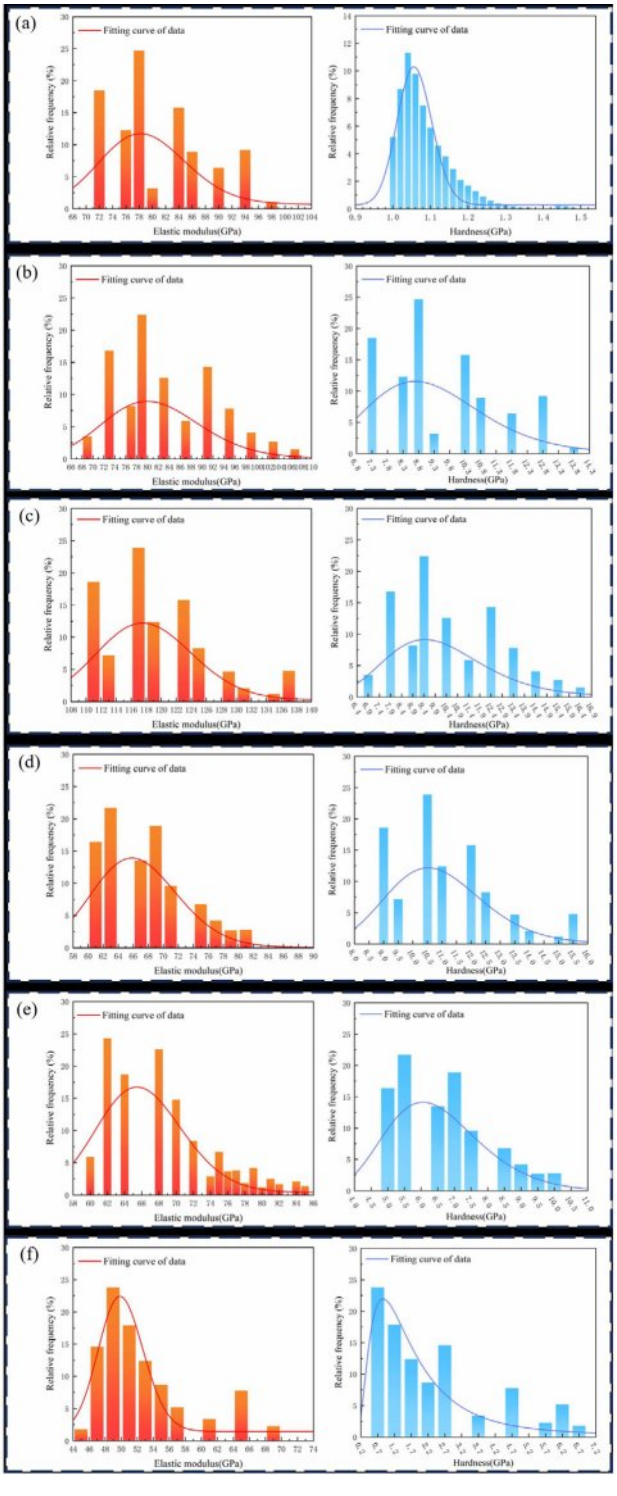

Fig. 11. Statistical analysis results of elastic modulus and hardness of samples with different content of spherical mullite powders: (a) 0 wt.%, (b) 6 wt.%, (c) 12 wt.%, (d) 18 wt.%, (e) 24 wt.%, (f) 30 wt.%.

spherical mullite powder is less than 12 wt.%, there is little difference in the micro mechanical parameters of different points within the micro-area of the sample, indicating that the sample has better and uniform mechanical properties. Further increasing the content of mullite not only leads to a decrease in micro mechanical properties, but also an increase in sample defects and non-uniformity, which significantly reduces its mechanical properties.

The micro zone hardness and elastic modulus of different samples calculated based on multi-point data are further presented in Fig. 10. Both parameters exhibited an initial enhancement followed by degradation with increasing mullite content. At the optimal 12 wt.% mullite incorporation, peak values of 130 GPa (elastic modulus) and 16 GPa (hardness) were achieved, representing significant enhancements of 33.8% and 31.3% respectively compared to reference specimens. In order to further improve the reliability of the data, statistical calculations were combined to further analyze the data. The results are shown in Fig. 11, and the data fitting results have the same trend of change as the test results, indicating the reliability of the test results.

It can be explained that the high intrinsic elasticity modulus (about 220 GPa) and Vickers hardness (about 15 GPa) of mullite phase can effectively improve the overall stiffness of the composite material when uniformly dispersed in the matrix. When the optimal amount is added, spherical mullite can be attributed to mechanisms such as function as nano-reinforcements through load transfer, mitigate residual stresses via thermal expansion coefficient mismatching between different phases to improve the micromechanics. The hardness reduction at 30 wt.% mullite content directly corresponds to the porosity increase documented in Fig. 3 and Fig. 4, confirming that excessive spherical mullite disrupting the continuity of the matrix, hindering the material transport and leading to incomplete sintering densification.

Fracture toughness

The fracture toughness and critical crack size of sintered porcelain insulators with varying spherical mullite additions are shown in Fig. 12. The critical crack size, defined as the maximum allowable defect dimension under maximum stress conditions, quantifies the material's capacity to withstand and dissipate strain energy. Both fracture toughness and critical crack size exhibited a characteristic of increase first and then decrease with increasing mullite content, reaching optimal values of 5.1 MPa·m$^{1/2}$ and 714 μm respectively at 12 wt.% spherical mullite addition. These values represent significant enhancements of 45.4% and 60.1% compared to reference specimens.

This behavior aligns with the Griffith fracture theory, where critical crack size demonstrates direct proportionality to fracture surface energy. The performance enhancement at 12 wt.% arises from three synergistic mechanisms: increased crack path tortuosity through columnar mullite induced deflection, enhanced crack bridging via well-dispersed spherical particles, improved energy dissipation through interfacial friction of different phases. When the amount of mullite added is small, a continuous crack blocking network is not formed. On the contrary, excessive mullite can lead to mullite agglomeration and an increase in porosity within the material.

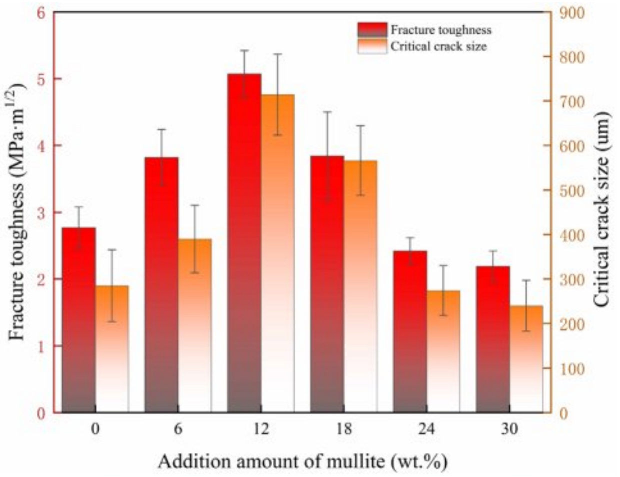

Fig. 12. Fracture toughness and critical crack size of the samples with different content of spherical mullite powders.

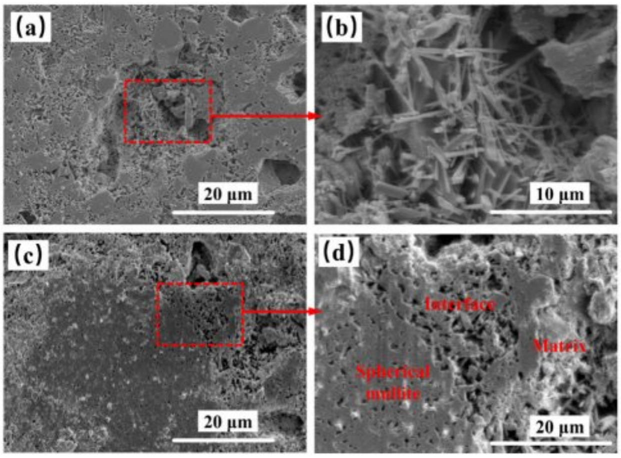

Fig. 13. SEM images of acid pickling samples: (a-b) S0, (c-d) S12.

Discussion

As previously discussed, within the spherical mullite addition range of 0-30 wt.%, appropriately increasing mullite content enhanced the sintering degree of specimens while reducing porosity and improving mechanical properties. However, excessive mullite additions induced particle agglomeration and caused excessive volume expansion, which compromised material homogeneity and consequently led to increased porosity and deteriorated mechanical performance. Especially, the elevated spherical mullite content accelerated the chemical reaction between Al_2O_3 and SiO_2 to form secondary mullite. The associated volume expansion during mullitization was identified as a critical factor influencing porosity evolution during the sintering process. The results demonstrated that specimens with 12 wt.% spherical mullite addition exhibited the lowest apparent porosity and best mechanical properties, including maximum compressive strength, flexural strength, Vickers hardness and fracture toughness.

Typically, microstructural characteristics play a pivotal role in determining material properties. However, the aforementioned analysis only compared densification degrees among different specimens through SEM, failing to comprehensively elucidate the influence of spherical mullite on material performance from the perspective of microstructural evolution. Therefore, establishing explicit correlations between microstructural and mechanical properties becomes imperative. Particularly for Al_2O_3-SiO_2-based porcelain insulators, the in-situ formation of mullite and its morphological characteristics constitute critical factors governing material performance.

In order to observe the morphological characteristics of mullite in the sintered sample more clearly, hydrofluoric acid was used to remove the glass phase on the surface of the sample, which was then used for SEM characterization. This chemical etching approach effectively exposes the mullite crystalline framework by dissolving the amorphous silicate matrix. The representative SEM images of HF pickled specimens, revealing distinct mullite morphological.

The SEM comparison images of samples with 0 wt.% and 12 wt.% addition of spherical mullite are shown in Fig. 13, it can be seen that all sintered samples developed acicular microstructural constituents. Columnar components appeared inside the spherical mullite sample. When the amount of spherical mullite added is 12 wt.%, a large number of columnar components interweave with each other at the interface between spherical mullite and matrix and an interpenetrating network was observed. Such microstructure-property relationships align with the measured mechanical performance of 12 wt.% spherical mullite added samples, such as flexural strength and fracture toughness, etc.

Table 4. EDS results at different positions in Fig. 13.

Point	Al (at%)	O (at%)	Si (at%)	C (at%)	Pt (at%)
1	9.44	45.20	3.54	17.28	24.53
2	15.41	61.32	5.67	7.81	9.78

To observe the mullite network structure in the interface of the spherical mullite added sample more clearly, the sample was observed at high magnification after acid pickling. The corresponding SEM and EDS results are shown in Fig. 14 and Table 4. According to the EDS results, the one-dimensional ceramic phase marked at points 1 and 2 is mullite. One dimensional mullite interpenetrates with other components in the sample, forming a well bonded network at the interface between spherical mullite and ceramic matrix, which is very beneficial for improving mechanical properties. During the material fracture process, one-dimensional mullite increases the fracture energy of the sample through pull-out, fracture, and bridging effects, resulting in a significant improvement in the toughness of the sample.

Furthermore, the crack propagation characteristics of cracks in the sample S12 was observed by SEM and shown in Fig. 15, where the sample was thermal shocked to introduce the more easily observable cracks. As shown in Fig. 15(b), the deflection and branching effect of spherical mullite on cracks can be clearly observed, and in Fig. 15(d), the strengthening and toughening effect of whiskers and in-situ generated whiskers in spherical mullite can be seen through fracture and bridging [34, 35].

As mentioned above, in order to more clearly

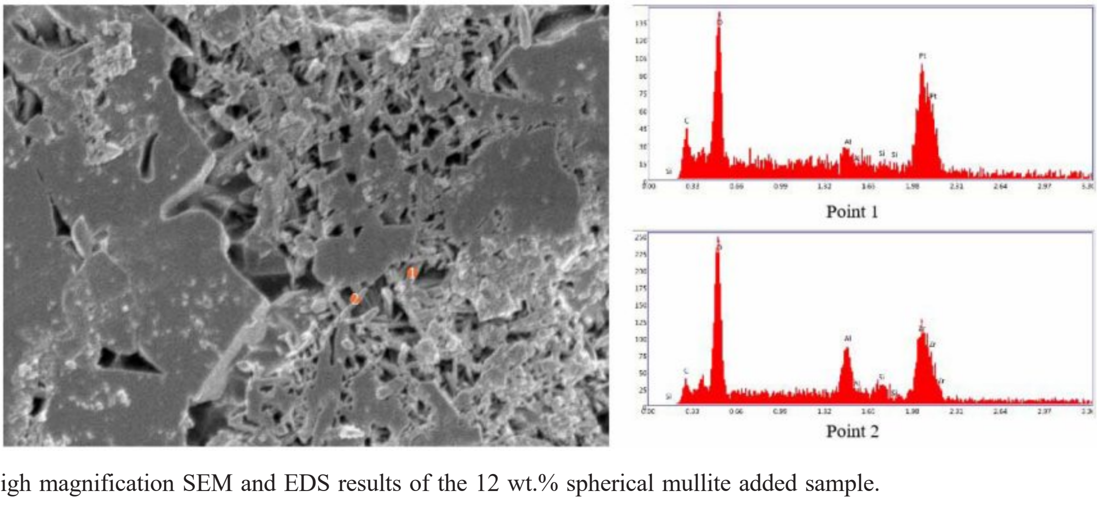

Point 1

Point 2

Fig. 14. High magnification SEM and EDS results of the 12 wt.% spherical mullite added sample.

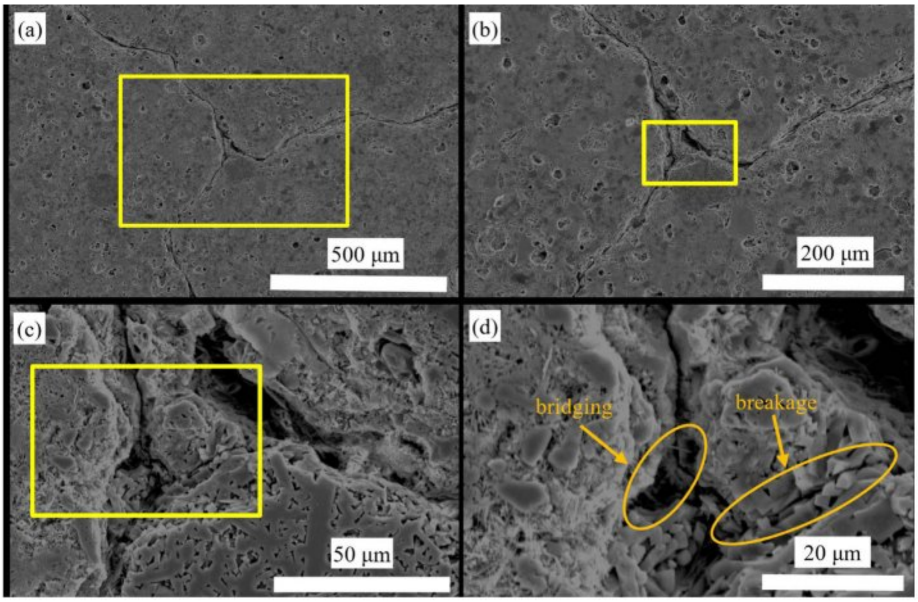

Fig. 15. SEM images of cracks in S12.

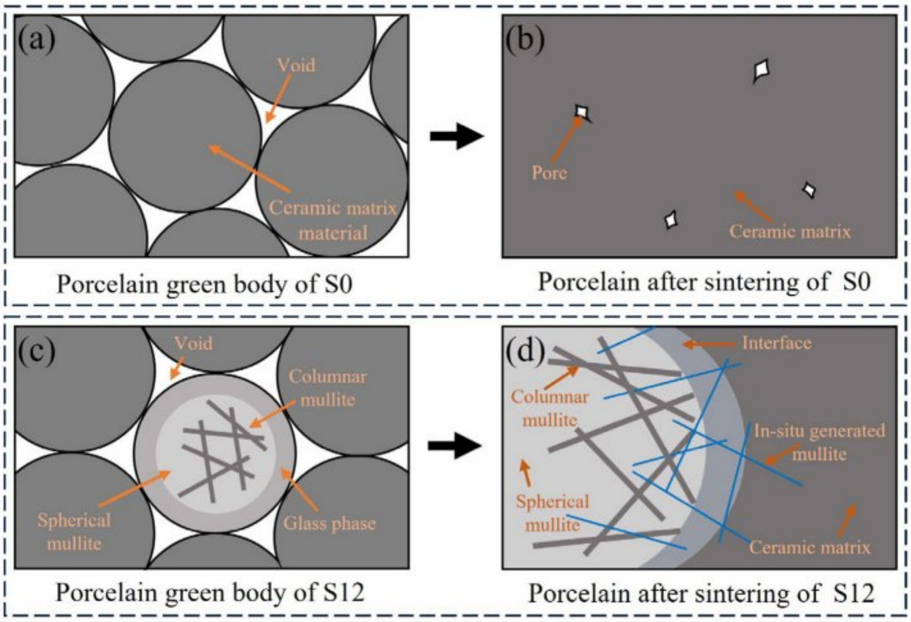

Fig. 16. Schematic diagram of spherical mullite regulated microstructure of insulators.

demonstrate the effect of introducing spherical mullite on the microstructure of porcelain insulator samples, a schematic diagram as shown in Fig. 16 is provided.

Conclusion

(1) The incorporation of spherical mullite powders significantly enhanced the mechanical properties of porcelain insulators. The 12 wt.% spherical mullite added samples exhibited optimal comprehensive performance, achieving the lowest apparent porosity (1.57%), the highest compressive strength (321 MPa) and flexural strength (107 MPa). Furthermore, they demonstrated superior fracture toughness (5.1 MPa·m$^{1/2}$) and maximum critical crack size (714 μm), representing a 45.4% and 60.1% improvement compared to the reference sample.

(2) The synergistic effects of glass phase filling and volume expansion during mullitization collectively reduced apparent porosity and enhanced mechanical properties. Specifically, in-situ generated columnar mullite at the interface between spherical mullite particles and the matrix interlocked with pre-existing mullite within

the spherical powders, forming a three-dimensional reinforcement network, which plays a key role in enhancing mechanical properties.

Author' Contribution Statement

Yonggang Yue: Conceptualization, Methodology, Supervision, Writing, Funding Acquisition; Xiaoyun Tian: Data Curation, Formal Analysis, Writing; Xiaochuan Chong: Experimental Work, Software, Writing, Original Draft Preparation; Donghai Ding: Resources, Review & Editing; Guoqing Xiao: Investigation, Validation, Writing, Review & Editing; Liming Wang: Project Administration, Data Interpretation, Writing; Bin Cao: Methodology, Project Administration, Writing; Lanjun Yang: Formal Analysis, Data Curation, Writing.

Funding

This work was supported by the Funding of 2024 Science and Technology Plan Project of Inner Mongolia Power Company (No. 2024-4-30, No. 2024-4-32).

Data availability

The data that support the findings of this study are available from the corresponding author upon reasonable request.

Acknowledgement

The authors acknowledge Ms. Yunqin Gao and Ms. Xing Hou, High-Temperature Ceramics Institute of Xi'an University of Architecture and Technology, for their assistance with the preparation and performance test of refractories.

Declarations

Competing interests The authors declare that they have no known competing financial interests or personal relationships that could have appeared to influence the work reported in this paper.

References

1. C. Gao, K. Luo, L. Li, J. Guo, M. Lu, and Z. Xu, J. Electr. Eng. Technol. 20[3] (2024) 1873-1885.
2. S. Sanyal, F. Aslam, T. Kim, S. Jeon, Y.J. Lee, J. Yi, I.H. Choi, J.A. Son, and J.B. Koo, Trans. Electr. Electro. 21[1] (2019) 16-21.
3. M. Asif, K.A. Soufi, U.A. Khan, and L.M. Alhems, IEEE Access 12 (2024) 38849-38866.
4. L. Lan, G. Zhang, Y. Wang, X. Wen, W. Wang, and H. Pei, IEEE Access 7 (2019) 121395-121406.
5. S. Simpy, T. Kim, J. Yi, K. Ja, S. Ju, and C. Hyuk, Appl. Sci. 10 (2020) 694-704.
6. U.A. Khan, K.A. Soufi, M. Asif, and L. Alhems, Eng. Fail. Anal. 166 (2024) 108876.
7. D. Zhang, Y. Zhang, H. Liu, Y. Cheng, W. Wan, T. Gao, X. Han, Z. Zhang, and X. Jiang, Electr. Pow. Syst. Res. 233 (2024) 110488.
8. A.K. Kaviraj, S. Saha, A. Chakraborty, G. Pahari, D. Ray, T.K. Parya, and S.K. Das, J. Aust. Ceram. Soc. 57[2] (2020) 327-337.
9. O. Gavalda, E. Saiz, J. Chevalier, and F. Bouville, Int. Mater. Rev. 70 (2025) 3-30.
10. O. Faruk, A.K. Bledzki, H.P. Fink, and M. Sain, Macromol. Mater. Eng. 299[1] (2014) 9-26.
11. W.M. Carty, and U. Senapati, J. Am. Ceram. Soc. 81[1] (2005) 3-20.
12. L. Carbajal, F.R. Marcos, M.A. Bengochea, and J.F. Fernandez, J. Eur. Ceram. Soc. 27[13-15] (2007) 4065-4069.
13. M. Esmaili, M.R. Nilforoushan, and M. Tayebi, Ceram. Int. 47[12] (2021) 17435-17444.
14. J.E. Contreras, J.T. Tijerina, J.F. López, F. Banda, L. Díaz, and E.A. Rodríguez, Mater. Chem. Phys. 263 (2021) 124389.
15. N.S. Mehta, S. Dey, and M.R. Majhi, Mater. Chem. Phys. 259 (2021) 124020.
16. R. Roy, D. Das, and P.K. Rout, Eng. Sci. 18 (2022) 20-30.
17. K. Cui, Y. Zhang, T. Fu, J. Wang, and X. Zhang, Coatings 10[7] (2020) 672.
18. H. Schneider, J. Schreuer, and B. Hildmann, J. Eur. Ceram. Soc. 28[2] (2008) 329-344.
19. Y. Zhao, Y. Fei, L. Du, H. Geng, X. Sun, X. Yin, and Z. Du, Ceram. Int. 51 (2025) 8843–8854.
20. H. Zhang, L. Yin, Q. Liu, Y. Chen, S. Jin, K. Xiao, H. Zhu, X. Zhang, and X. Wu, Appl. Clay Sci. 232 (2023) 106766.
21. Y. Yue, L. Yang, X. Chong, G. Xiao, and D. Ding, J. Aust. Ceram. Soc. (2025). DOI:10.1007/s41779-025-01203-1
22. X. Wang, A. Guo, J. Liu, Y. Wang, J. Liu, H. Du, and F. Hou, Ceram. Int. 42[11] (2016) 13161-13167.
23. Z. Liu, C. Wu, N. Xie, J. Zhu, Y. Liu, S. Huang, X. Shen, Z. Yang, X. Lin, and L. Kong, Int. J. Appl. Ceram. Tec. 19[3] (2022) 1659-1668.
24. H. He, G. Shao, R. Zhao, H. Tian, H. Wang, B. Fan, H. Lu, H. Xu, R. Zhang, and L. An, Adv. Ceram. 12 (2023) 321-328.
25. G. Chen, F. Yang, S. Zhao, K. Li, J. Chen, Z. Fei, and Z. Yang, Ceram. Int. 48[13] (2022) 19367-19374.
26. X. Chen, T. Li, Q. Ren, X. Wu, H. Li, A. Dang, T. Zhao, Y. Shang, and Y. Zhang, J. Alloy. Compd. 700 (2017) 37-42.
27. X. Chen, T. Li, Q. Ren, X. Wu, A. Dang, H. Li, and T. Zhao, J. Alloy. Compd. 729 (2017) 285-292.
28. P. Zhao, S. Ma, X. Wang, W. Wu, and Y. Ou, Ceram. Int. 49[7] (2023) 10238-10248.
29. M. Yang, J. Li, Y. Man, Z. Peng, X. Zhang, and X. Luo, J. Asian Ceram. Soc. 8[2] (2020) 387-395.
30. X. Chen, S. Li, Y. Shang, J. Wang, and J. Zheng, Process. Appl. Ceram. 18[1] (2024) 77-86.
31. F.O. Aramide, and A.P. Popoola, J. Ceram. Process. Res. 19[2] (2018) 87-94.
32. L. Zhang, H. Wu, Z. Liu, Y. Yang, H. Liu, X. Wu, B. Pei, J. Han, and Z. Huang, Ceram. Int. 51[22] (2025) 37157-37168.
33. X. Chong, J. Luo, D. Ding, S. Jin, and G. Xiao, J. Am. Ceram. Soc. 106[11] (2023) 6891-6910.
34. Y. Yang, A. Wang, Y. Zhou, X. Li, R. Zhao, S. Niu, and X. Xu, Ceram. Int. 51[10] (2025) 12622-12633.
35. M. Tian, Q. Yang, Y. Yu, Y. Zheng, F. Liu, and X. He, J. Eur. Ceram. Soc. 45[6] 2025 117148.